

# Enhanced Patch-wise Maximal Intensity Prior for Deblurring Neutron Radiographic Images

Original Scientific Paper

## K. Yazid

Malaysian Nuclear Agency, Technical Support Division,  
43000 Bangi, Selangor, Malaysia  
khairiah Yazid@gmail.com

## H. Ibrahim

Universiti Sains Malaysia, School of Electrical and Electronic Engineering Campus,  
14300 Nibong Tebal, Penang, Malaysia  
haidi@usm.my

## Mohd Zaid Abdullah\*

Universiti Sains Malaysia, School of Electrical and Electronic Engineering Campus,  
14300 Nibong Tebal, Penang, Malaysia  
mza@usm.my

\*Corresponding author

**Abstract** – In neutron radiographic imaging, generally, the collimation ratio is assumed to be sufficiently large to ensure a valid approximation for parallel beam geometry. However, this assumption is difficult to apply in small nuclear reactors due to the low-intensity neutron flux. For this reason, these reactors produced inherently blurry neutron images. In this paper a blind deconvolution technique is investigated for the enhanced visual quality of neutron images through the reduction of blurring artefacts. Technically, this approach is extremely challenging because it requires an unknown point spread function. To solve this problem, scholars employ the gradient minimization strategy under the framework of a maximum a posteriori, which leads to the development of an improved deblurring method, referred to in this paper as the enhanced patch-wise intensity prior. Experimental results demonstrate that the high competitiveness of the proposed method in terms of blind or no-reference evaluation measure, with an average of 46.1 for six neutron images used in this study. This value is considerably lower compared with those of existing deblurring techniques, which implies a more accurate restoration. Additionally, the proposed method resulted in the highest, and hence, the best entropy and contrast values, averaging at 7.09 and 1.05 respectively. The proposed method is also the second fastest technique with a mean time of 180 s.

---

**Keywords:** Image Restoration, Point Spread Function, Blind Deconvolution, Neutron Radiography, Collimation Ratio

---

Received: July 17, 2024; Received in revised form: October 7, 2024; Accepted: October 4, 2024

## 1. INTRODUCTION

Neutron radiography (NR) uses neutron radiation to probe the internal structures of objects, and it shows similarity to X-ray radiography. However, different from X-ray, neutrons are easily attenuated by light elements, such as hydrogen and boron, but can easily penetrate numerous heavy metals. These unique properties render NR a highly useful technique for nondestructive testing and quality control inspection. Despite being powerful and unique, the NR images produced by low-power nuclear reactors exhibit inherent degradation due to blurring. Examination of the collimation system, which is one of the core elements in NR image capture,

can be used to explain the main source of blurring (Fig. 1). Referring to this figure the collimator system, which comprises an aperture and detector, directs a neutron beam to an object. Similar to a pinhole camera, the aperture prevents neutrons from entering the beam except through the hole, which concentrates neutrons within a small area, and hence reduces image distortion and chromatic aberration. Meanwhile, the detector converts neutrons into a two-dimensional (2D) image that depicts the internal structure of an object. This geometry determines the collimation ratio, which is an important characteristic of NR. In this case, the collimation ratio refers to the ratio of collimation length  $L$  to the effective diameter of the aperture  $D$  or  $L/D$ .

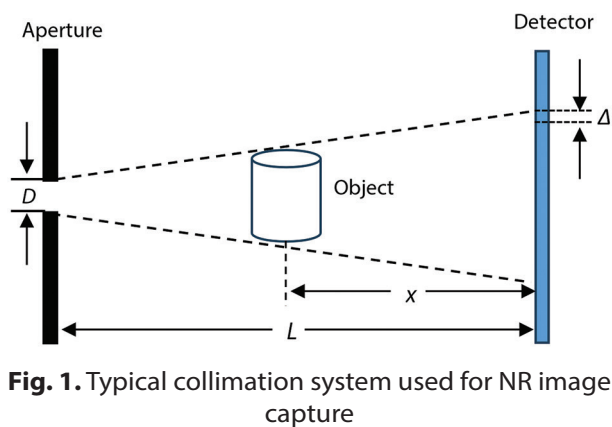


**Fig. 1.** Typical collimation system used for NR image capture

Following the pinhole camera analogy, geometric blurring can be defined as  $\Delta = x / (L/D)$ , where  $\Delta$  directly determines the resolution or sharpness of NR images. An optimal resolution is obtained when  $\Delta \rightarrow 0$ . This requirement can be attained either through placement of the object close to the detector ( $x \rightarrow 0$ ) or with the use of a larger collimation ratio ( $L/D \rightarrow \infty$ ). However, the contrast exhibits a rapid drop with the decrease in  $x$  due to the reduced intensity of neutron flux through an inverse-square relationship. For this reason,  $x$  is maintained at a reasonable distance, whereas  $L/D$  is maintained as high as possible to produce NR images with adequate contrast and acceptable resolution. Typically, the  $L/D$  of high-power neutron reactors ranges between 125 to 500 [1]. By contrast, the  $L/D$  of small reactors are generally considerably lower than this range. At Malaysia Nuclear Agency (MNA), the  $L/D$  of NR facilities approximates 105, which is moderately low compared with those of high-power or large-scale reactors. Using an arctan inverse relationship (i.e.  $(\tan^{-1}(1/(L/D)))^{-1}$ ) this ratio is equivalent to a beam divergence of approximately  $1.82^\circ$ . The low  $L/D$  or high beam divergence serves as the primary cause of the blurring for images captured at this facility. Hence, image deblurring or restoration constitutes one of the important tasks in post image processing activities in this reactor. For linear, shift-invariant systems, image restoration can be modeled as a convolution operation. Mathematically:

$$B = k * L + n \quad (1)$$

where  $B$  represents the blurred image,  $L$  refers to an unknown latent or sharp image,  $k$  denotes the PSF,  $*$  represents the 2D convolution operator and  $n$  corresponds to additive noise. In most deblurring applications,  $n$  can be ignored because it is small and uncorrelated. Given that  $k$  is generally unknown, the image restoration methods transforms into a blind-deconvolution problem. Among all available solutions to this problem, the maximum a posteriori (MAP) is the most popular and widely used technique. An earlier work in this field is a paper published elsewhere [2]. Their algorithm is effective when dealing with small-sized images and hence less complex PSFs. Multilayer iterative estimation techniques are usually deployed for large images with relatively complex PSFs. Importantly, this algorithm exhibits sensitivity

to local minima, which led to inaccurate estimation of PSF and in turns affected the deblurring results. Hence, regularization is performed to increase the probability of finding good local minima. In general, this step is introduced into an optimization problem to prevent overfitting and reduce complexity [3, 4]. They developed an  $L_0$ -based image smoothing algorithm by retaining large structures and removing minute details. They used  $L_0$  and  $L_2$  norms for image gradient prior and kernel prior, respectively. However, such an algorithm is time consuming because the solutions require solving a complicated joint optimization problem. Moreover, it requires sophisticated priors and thus considerably more complex optimizers. Therefore, the superior performance of this method is compromised by a high computational cost. These problems were addressed, which resulted in development of an improved technique [5]. These authors assumed that not all edges in the latent image are significant and useful. This assumption allowed them to enforce  $L_0$  regularization to constrain the sparsity of image prior and use  $L_2$  to regularize the kernel prior. Such regularization strategies not only improve the quality of image deblurring but also reduce the runtime. A new channel prior called the enhanced local maximum intensity has also been investigated [6]. Though effective, however, this algorithm has only been tested in the restoration of text documents with a uniform background. Compared with text images, NR images exhibit a more complex intensity distributions because they contain many brightly illuminated pixels due to the strong penetration of neutrons. Therefore, the direct application of intensity priors is less satisfactory for NR images. In another work. In another research a sparse prior based on a collection of local minimal pixels in non-overlapping patches has been proposed [7]. Referred to as patchwise minimal pixels (PMPs), this method involves the calculation of the low intensity of dark pixels in non-overlapping patches. Despite the remarkable performance of this method, especially when an image contains many dark pixels, its effectivity decreases when dealing with large-sized images or complex PSFs. Solving this method led to the development of a new sparse channel prior that considers the relationship between dark and bright channel priors [8]. Even though the authors reported improved performance, however, the method is very time consuming as it requires more than 115 s to process a small image with a size of  $256 \times 256$  pixels. Recently, the deep learning approach for restoring neutron image has also been reported [9,10]. However, due to the unavailability of standard neutron image dataset, the authors have resorted to using X-ray images as substitutions for training and testing. Though the results are quite promising, however, it's difficult to evaluate the actual performance of the algorithm because of different type of images used in the investigation.

Following the above discussion, this paper proposes an alternative strategy based on high-intensity bright pixels. It also addresses large and complex PSFs as evident from the ensuing discussion. The basic idea be-

hind this idea is first published at a conference meeting held recently [11]. Following this publication, this paper presents detailed information of the proposed method including the use of a much more efficient and accurate PSF estimator. Compared to the trial-and-error method as in our previous publication, here, a more systematic approach in determining important parameters of the algorithm is devised and discussed. Also the performance of the proposed solution is evaluated critically by comparing results with the state-of-the-art methods. Our contributions are as follows:

1. A new effective and simple image prior that uses bright pixels in nonoverlapping patches. This new image prior is referred to as the enhanced patch-wise intensity (EPI).
2. A new cost-effective penalty function to enforce sparsity of the prior. During induced sparsity, the regu-

larization term facilitates recovery of sharp images, which are in turn used in PSF estimation. The method helps in accelerating the runtime because only the nonzero elements are used in the computation.

## 2. MATERIALS AND METHODS

### 2.1. INTENSITY DISTRIBUTIONS

In consideration of the above discussion, two important assumptions are accounted for in the method proposed in this paper. First, most NR images contain a high number of brightly illuminated pixels, which is principally due to intense radiation, with neutrons easily penetrating most objects except hydrogenated materials. Second, brightly illuminated pixels show a drop in intensity due to blurring. Fig. 2 illustrates these assumptions using three different NR images.

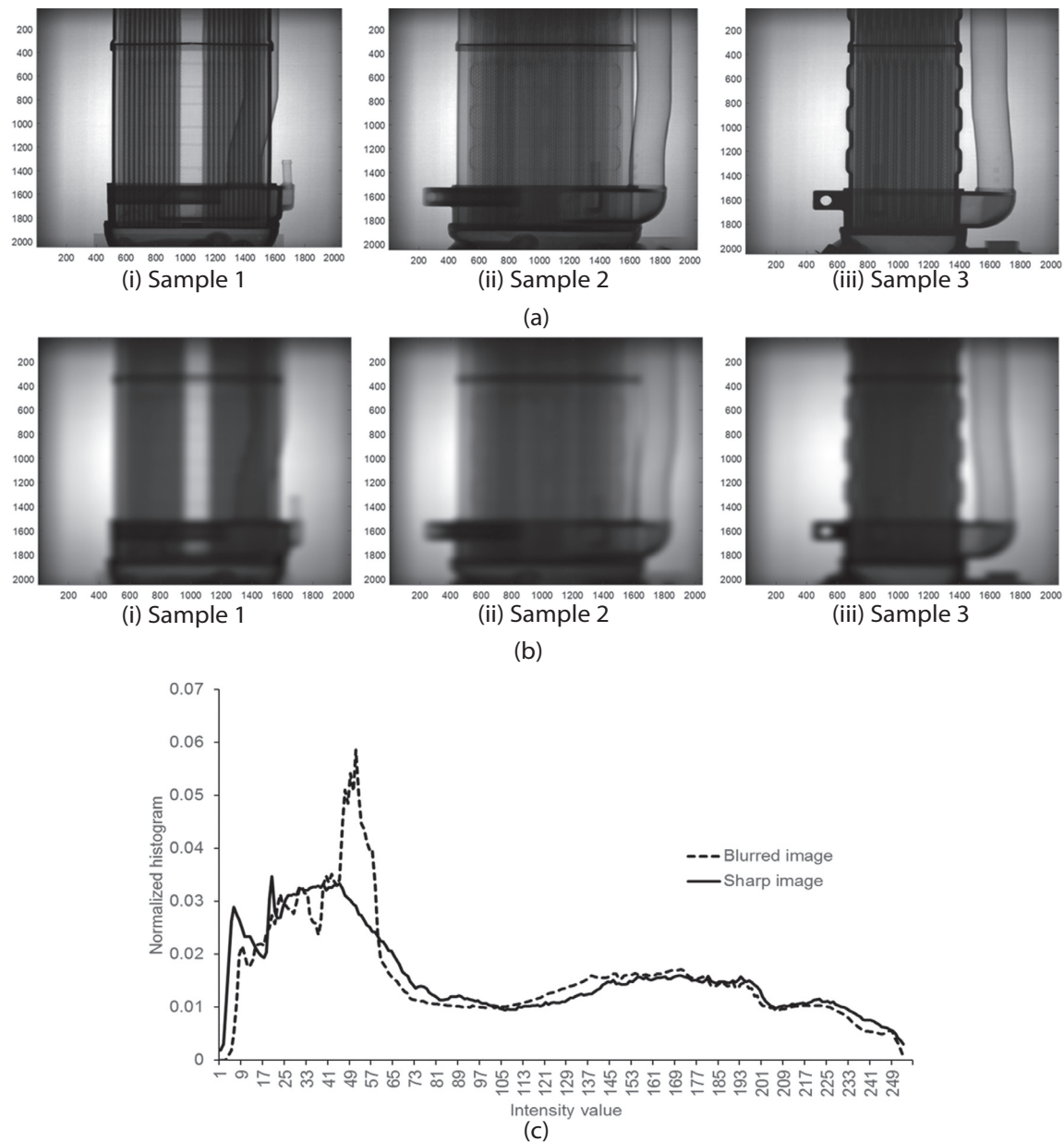


**Fig. 2.** The effect of blurring on image brightness and intensity distributions. (a) Sharp images, (b) Blurred images, (c) Histogram

The images in Fig. 2(a) appear sharp and clear because they are captured using a high-power nuclear reactor. In this case, Figs. 2(a)(i-iii) include the original sharp images captured from three different projections, and Figs. 2(b)(i-iii) display their corresponding blurry counterparts. Blurring is simulated using a simple low-pass filter. Comparison of Figs. 2(a) and 2(b) shows the reduction in brightness after blurring, which implies the considerable drop in intensity. To further prove this observation, we examined the characteristics of sharp and blurred images on their histograms. In so doing the probability density function (PDF) for sharp and blurry images are first calculated, second normalized, and then averaged. Fig. 2(c) displays the results. As shown in the figure, the histogram of blurred image shift to the left, which results in more pixels occupying low gray-scale values and implies the reduced image brightness due to blurring.

## 2.2. ENHANCED PATCH-WISE INTENSITY PRIOR

On the basis of the above assumptions, the proposed prior employs high-intensity bright channel pixels in non-overlapping patch. The proposed method can be explained by referring to a sharp image  $L$  of size  $m \times n$  and partitioned into  $d$  non-overlapping patches; with each size  $r \times r$ , the patch size  $r$  can be varied by ratio formula:  $r=SF \times ((m+n)/2)$  where  $SF$  is a scaling factor. Meanwhile  $d=[m/r] \times [n/r]$ , and  $[\cdot]$  denotes the ceil operator. For gray scale image the EPI prior can be defined as follows:

$$EPI(L)(i) = \max_{(x,y) \in \Omega_i} L(x,y) \quad (2)$$

where  $(x, y)$  denotes the pixel coordinates, and  $\Omega_i$  denotes the  $i$ -th non-overlapping patch with  $i=1,2,\dots,d$ . Therefore,  $EPI(L)(i)$  represents the collection of high-intensity or bright pixels of  $i$ -th non-overlapping patch. Similarly, the EPI prior of blurred image  $B$  can be expressed as follows:

$$EPI(B)(i) = \max_{(x,y) \in \Omega_i} B(x,y) \quad (3)$$

As discussed previously, the brightness of an image drops as a result of blurring. Hence, the EPI prior of the blurred image is much less than that of a sharp latent image. Mathematically, the following inequality holds:

$$EPI(B) \leq EPI(L) \quad (4)$$

Substituting Equation (1) into Equation (4) gives

$$\max_{(x,y) \in \Omega_i} B(x,y) = \max_{(x,y) \in \Omega_i} L(x,y) * k \quad (5)$$

where  $k>0$  and  $\sum k=1$ . Following Equations (4) and (5), the maximum intensity value of a blurred image is also significantly less than that of a sharp image. With the assumption that the patch size for  $B$  and  $L$  is the same, the following inequality is also valid:

$$\max_{(x,y) \in \Omega_i} B(x,y) \leq \max_{(x,y) \in \Omega_i} L(x,y) \quad (6)$$

As explained, this paper exploits high-intensity pixels to distinguish sharp from blurry images. With this assumption, the deblurring model is developed and presented in the following subsections.

## 2.3. DEBLURRING MODEL

With the use of Equation (1), the deblurring model based on the standard MAP estimation framework is developed as follows:

$$\min_{L,k} \|L * k - B\|_2^2 + \gamma P(L) + \mu P(k) \quad (7)$$

The first term  $\|L * k - B\|_2^2$  is a data fidelity term that constrains the convolution of  $L$  and  $k$  so that the result is consistent with  $B$ . The regularized terms  $P(L)$  and  $P(k)$  are priors related to latent image and PSF kernel, respectively.  $\mu$  and  $\gamma$  are positive regularizing parameters that balance the weight relation between the fidelity and priors. The deblurring problem is non-convex; therefore, regularization helps constrain the priors to increase the probability of producing a good local solution. As explained previously, the gradient of a natural image is sparse. Consequently,  $P(L)$  is regularized such that

$$P(L) = \|L\|_0 \quad (8)$$

where  $\|\cdot\|_0$  indicates the zero norm. Meanwhile, the kernel prior is formulated as

$$P(k) = \|k\|_2^2 \quad (9)$$

where  $\|\cdot\|_2$  denotes the second norm. The deblurring model can be formulated by combining Equations (8) and (9). Mathematically,

$$\min_{L,k} \|L * k - B\|_2^2 + \mu \|\nabla L\|_0 + \gamma \|k\|_2^2 \quad (10)$$

where  $\nabla = (\nabla_h, \nabla_v)$  denotes the image gradients calculated in the horizontal and vertical directions. In this case the  $\|\cdot\|_2$  is also used to constraint the data term because this norm is known to be optimal for Gaussian noise. Moreover it enables the solution to be calculated using a standard fast Fourier transform (FFT) algorithm. Introducing the EPI, Equation (10) can be rewritten as:

$$\min_{L,k} \|L * k - B\|_2^2 + \gamma \|k\|_2^2 + \mu \|\nabla L\|_0 + \alpha \|EPI(L)\|_0 \quad (11)$$

where  $\alpha$ ,  $\mu$ , and  $\gamma$  are positive weight parameters. Traditionally, an iterative-based Half Quadratic Splitting (HQS) algorithm is used in solving Equation (10), such as in [5] and [10]. However, this algorithm is complex and time consuming. Thus, an alternative strategy is employed in this study. Exploiting the sparsity of the EPI in non-overlapping patch, Equation (9) is solved directly via soft thresholding. The following condition is introduced to constrain the solutions in such a way that

$$\min_{L,k} \|L * k - B\|_2^2 + \mu \|\nabla L\|_0 + \gamma \|k\|_2^2 \quad (12)$$

subject to  $EPI(L)(i) \sim p(x)$ , for  $i \in \{1, \dots, d\}$

where  $p(x)$  is a PDF. The thresholding of the minimum and maximum pixels of non-overlapping patches with a constraint value of 0.9 produces distributions whose shape is approximately hyper-Laplacian. This type of output together with the sparsity of high-intensity pixels enhances the distinguishability between sharp from blurred images. The next step is applying the alternating optimization rule to Equation (12), which splits the cost function into two subproblems. The first subproblem characterizes  $L$  using the following cost function:

$$L = \min_L \|L * k - B\|_2^2 + \mu \|\nabla L\|_0 \quad (13)$$

subject to  $EPI(L)(i) \sim p(x)$ , for  $i \in \{1, \dots, d\}$

The second subproblem describes the unknown  $k$  as follows:

$$k = \min_k \|\nabla L * k - \nabla B\|_2^2 + \gamma \|k\|_2^2 \quad (14)$$

Equations (13) and (14) are principally non-convex. Hence, the ideal solution may not exist. Therefore, these equations are solved through the minimization technique to produce approximate solutions. In so doing, similar approaches published by [5], [7], [12] and [13] are adopted. Interested readers are referred to these publications for further details. A summary of the minimization procedures is presented for the sake of completeness and thoroughness of discussion. The first step in the minimization process is to estimate  $k$ . The Gaussian function is used as a first estimate of  $k$  because the blurring is essentially low-pass filtering. Then, Equations (13) and (14) are solved alternately using methods and procedures discussed in the following subsections.

## 2.4. L SUB-PROBLEM

In solving Equation (13), a constraint is imposed to induce the sparsity on  $EPI(L)$ , indirectly speeding up the minimization process. Given a previous estimation of  $k^i$ , the latent image is updated via iterative thresholding. Mathematically,

$$L^{i+1} = \min_L \|L * k^i - B\|_2^2 + \mu \|\nabla L\|_0 \quad (15)$$

subject to  $EPI(L)(i) \sim p(x)$ , for  $i \in \{1, \dots, d\}$

Equation (14) comprises two important regularizers:  $L_2$  and  $L_0$ . The data fidelity term is smooth and convex, whereas the gradient term is non-convex. With the use of an auxiliary variable  $G$  with respect to the image gradient  $\nabla L$ , Equation (15) is reformulated to yield

$$\min_{L,G} \|L * k^i - B\|_2^2 + \beta \|\nabla L - G\|_2^2 + \mu \|G\|_0 \quad (16)$$

subject to  $EPI(L)(i) \sim p(x)$ , for  $i \in \{1, \dots, d\}$

where  $\beta$  is a positive and sufficiently large penalty parameter to enforce  $\|\nabla L - G\|_2^2 \approx 0$ , and  $\nabla L \approx G$ . As a result of additional constraints,  $L$  and  $G$  cannot be solved directly using popular algorithm such as the block

coordinate descent. Similar to [7], an alternative soft thresholding technique is applied to solve Equation (16) iteratively. The EPI subset of  $L^{t,j}$  is denoted as  $L_s^{t,j} := EPI(j)$  for  $t^{\text{th}}$  latent image at  $j^{\text{th}}$  iterative step, then the subsequent latent image is calculated by direct thresholding as follows:

$$\tilde{L}_s^{t+1,j}(i) = \begin{cases} 0, & |L_s^{t+1,j}(i)| < \lambda \\ L_s^{t+1,j}(i), & \text{else} \end{cases} \quad (17)$$

for  $i \in \{1, \dots, d\}$

where  $\lambda$  is the thresholding value, which is greater than zero. With  $\Omega^{t+1,j}$  denoted as the index set of EPI, the binary mask corresponding to EPI subset is calculated as follows:

$$M^{t+1,j}(i,j) = \begin{cases} 1 & \text{if } (i,j) \in \Omega^{t+1,j} \\ 0 & \text{else} \end{cases} \quad (18)$$

where  $M \in R^{m \times n}$  is the binary mask corresponding to the EPI subset of  $L$ . Here  $EPI(L): R^{m \times n} \rightarrow R^d$ ; thus, the inverse of  $EPI(L)$  is equivalent to  $EPI^T(L): R^d \rightarrow R^{m \times n}$  for any  $z \in R^d$ . Consequently,  $L$  can be presented by:

$$L_s := EPI^T(EPI(L)) = L \circ M \quad (19)$$

where  $\circ$  is the dot product. In this case  $M(i,j)=1$  is the maximal pixel in the non-overlapping patch. For other pixels,  $M(i,j)=0$ . With the use of the results of Equation (19), the intermediate latent image at  $j^{\text{th}}$  iterative step is updated as follows:

$$\tilde{L}^{t+1,j} = L^{t+1,j} \circ (1 - M^{t+1,j}) + EPI^T(\tilde{L}_s^{t+1,j}) \quad (20)$$

Substituting Equation (20) into Equation (16), the gradient subproblem of  $G$  is reformulated as follows:

$$G^{t+1,j+1} = \min_G \beta \|\nabla \tilde{L}^{t+1,j} - G\|_2^2 + \mu \|G\|_0 \quad (21)$$

where  $\nabla = (\nabla_h, \nabla_v)$  and  $G = (G_h, G_v)$ .  $G_h$  and  $G_v$  are the image gradient in the horizontal and vertical directions, respectively. Following [5], Equation (21) is solved using proximal minimization. Mathematically,

$$G^{t+1,j+1} = \begin{cases} 0, & (\nabla \tilde{L}^{t+1,j}(i,j))^2 < \mu/\beta \\ \nabla \tilde{L}^{t+1,j}(i,j), & \text{else} \end{cases} \quad (22)$$

Using results calculated from Equation (22), the final update formula for  $L$  is defined as follows:

$$L^{t+1,j+1} = \min_L \|k^i * L - B\|_2^2 + \|\nabla L - G^{t+1,j+1}\|_2^2 \quad (23)$$

The closed-form solution of Equation (23) can be obtained using the FFT algorithm. Mathematically,

$$L^{t+1,j+1} = \mathcal{F}^{-1} \left( \frac{\mathcal{F}(k^i) \mathcal{F}(B) + \beta (\mathcal{F}(\nabla_h) \mathcal{F}(G_h^{t+1,j+1}) + \mathcal{F}(\nabla_v) \mathcal{F}(G_v^{t+1,j+1}))}{\mathcal{F}(k^i) \mathcal{F}(k^i) + \beta (\mathcal{F}(\nabla_h) \mathcal{F}(\nabla_h) + \mathcal{F}(\nabla_v) \mathcal{F}(\nabla_v))} \right) \quad (24)$$

where  $F(\cdot)$  and  $F^{-1}(\cdot)$  denote FFT and inverse FFT, respectively.  $\overline{F(\cdot)}$  is the complex conjugate operator.  $\nabla_v, \nabla_h$

represent vertical and horizontal differential operators, respectively.

### 2.5. K SUB-PROBLEM

The  $k$  subproblem is solved in the gradient space, similar to the approach of [5], [10] and [11]. The update formula for  $k$  is given by

$$k^{i+1} = \min_k \|\nabla L^i * k - \nabla B\|_2^2 + \gamma \|k\|_2^2 \quad (25)$$

As before, the solution to Equation (24) is obtained through the FFT algorithm. The result is as follows:

$$k^{i+1} = \mathcal{F}^{-1} \left( \frac{\overline{\mathcal{F}(\nabla_h L^i)} \mathcal{F}(\nabla_h B) + \overline{\mathcal{F}(\nabla_v L^i)} \mathcal{F}(\nabla_v B)}{\overline{\mathcal{F}(\nabla_h L^i)} \mathcal{F}(\nabla_h L^i) + \overline{\mathcal{F}(\nabla_v L^i)} \mathcal{F}(\nabla_v L^i) + \gamma} \right) \quad (26)$$

The above optimization procedures are implemented using coarse-to-fine multi-scale structure. In this way,  $k$  is always non-negative, thus fulfilling the constraint requirement. The main steps involved in solving  $L$  and  $k$  subproblems are summarized in Appendix I.

Respectively the algorithm is named as Algorithm 1 and Algorithm 2. Referring to Algorithm 1, the method performs two-layer loop iterative calculations. Theoretically,  $\beta$  must be large for the algorithm to work.

However, a large  $\beta$  means that regularization is a time-consuming process. One solution to this problem is to first use smaller  $\beta$  and then iteratively update this figure until it reaches a stable target value. For this method to work,  $a > 1$ . In this research, the following parameters are chosen for Algorithm 1:  $a=2$ ,  $\beta_0=2\mu$ ,  $\beta_{max}=10^5$ ,  $\mu=4 \times 10^{-3}$ ,  $J=3$ . The threshold value  $\lambda$  is initially set to 0.1. This value is reduced gradually until it equals a mean value of EPI. Here  $\beta_0$  determines the starting strength of the regularization. Meanwhile,  $\beta_{max}$  is set to an upper limit to ensure a controlled regularization.

Together, they prevent excessive deblurring while preserving important details and avoiding over-smoothing.

### 2.6. IMPLEMENTATION

The alternate minimization described in Equations (24) and (26) iterates between latent image and kernel estimation. The blurred image and Gaussian function are used as first-guess solutions for  $L$  and  $k$ , respectively. Large kernels are estimated using the multilayer pyramid scheme combined with iterative minimization strategy. The scheme prevents optimization from being isolated in a local minimum. The strategy works gradually from the coarsest layer to the finest layer. Fig. 3 summarizes the working principle of the proposed method.

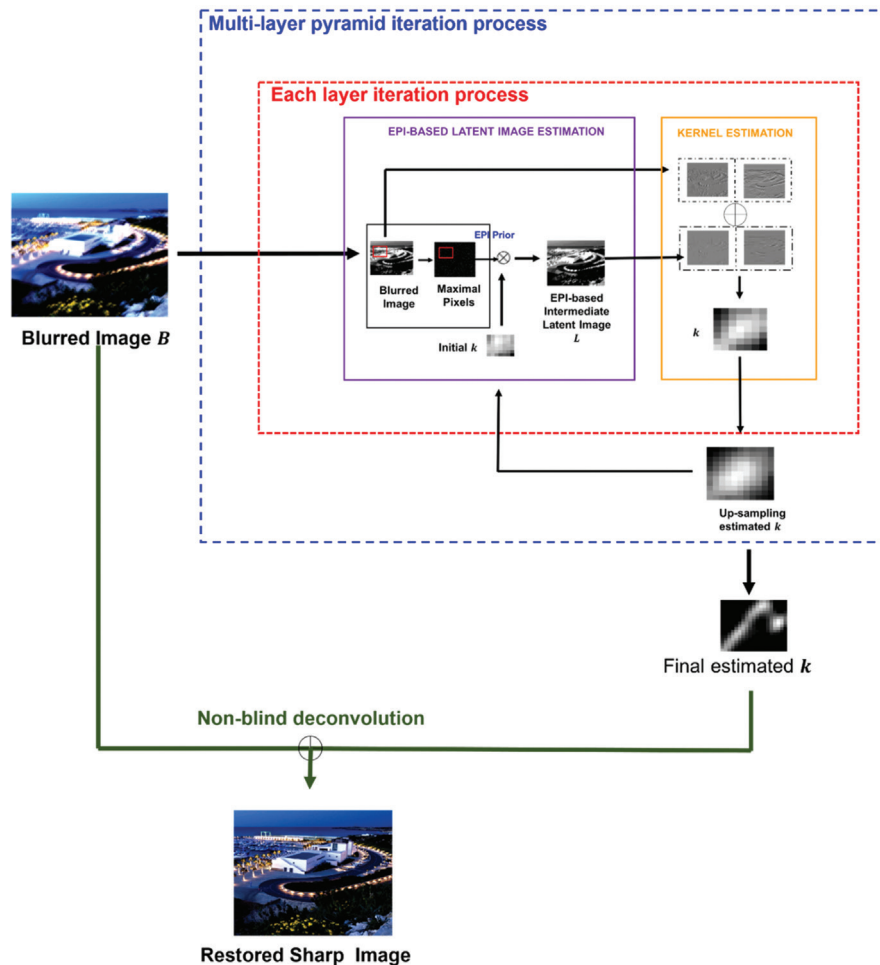


Fig. 3. Overview of the proposed EPI method

The figure shows the multilayer PSF processing unit represented by several elements inside the blue dotted square. The red-dotted rectangle refers to a single-layer pyramid PSF processing unit. In the unit, the square block on the left is the latent image calculation engine, and that on the right is the PSF estimator unit. Once  $k$  and  $L$  have been estimated in the low-resolution layer,  $k$  is upscaled for the next layer.  $L$  and  $k$  are refined iteratively in each layer. In this study, the maximum number of iterations is rigidly fixed to five. This value is selected heuristically because it produces the best solutions for all images used in the present work. During operation, the input image is first transformed into a grayscale one and then downscaled a few times. Here, the extent of downscaling depends on the size of the input PSF, which also determines the number of pyramid layers. The PSF size is used in the retrieval of a part of the kernel alone, which prevents noise accumulation in subsequent estimation processes.

Referring again to Fig. 3, in the minimization process, the blurred image is deconvoluted using the  $k$  estimated from previous iteration. The size of  $k$  in the coarsest layer is rigidly fixed to  $7 \times 7$ . At the start of minimization, weight  $\mu$  is set to a high value to ensure restoration of strong edges and removal of details. During each iteration cycle, a coarse  $L$  is computed with an EPI prior for each nonoverlapping patch. Theoretically, the EPI prior shows increased sparsity. Hence,  $L$  exhibits more details with the increase in the number of layers.

The orange rectangular block in Fig. 3 contains the kernel estimation algorithm. The weight parameter  $\gamma$  in Equation (26) is constantly set to a positive value to penalize large Fourier coefficients, which ensures a smooth PSF distribution. Then, the estimated  $k$  is up-scaled by a factor of 2, and the result serves as the initial prediction for the next estimation layer. The procedure is repeated until the intended size of  $k$  is reached. Equation (26) is solved, and all negative-value pixels in  $k$  are set to zero, centered, and finally normalized to 1.

The  $k$  estimated from a previous step is used in image restoration, with the blurred image serving as input. The restoration is non-blinded; therefore, such a problem can be solved using various image deconvolution techniques. In this paper, the algorithm published in [12] is utilized because this method produces few ringing artifacts and accurate restoration. Appendix II shows the complete procedure of the proposed EPI algorithm. The methods and procedures are implemented in MATLAB2023a. This software is installed in personal computer which housed 4.0 GHz Intel Core i5 processor, 8 GB RAM and Windows 11.

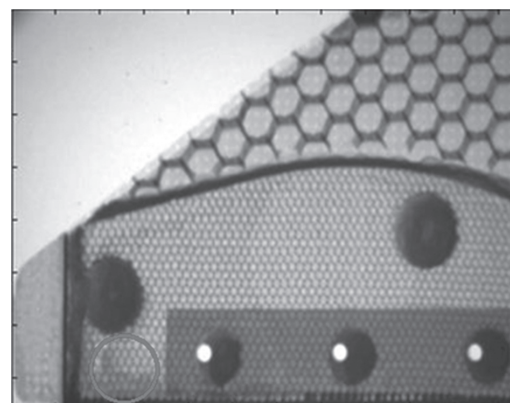
### 3. IMAGE ACQUISITION

Neutron imaging experiments are performed at MNA, which houses the Research TRIGA PUSPATI (RTP) reactor. The RTP is a swimming pool-type, light, water research reactor containing enriched uranium–zirconium–hydride

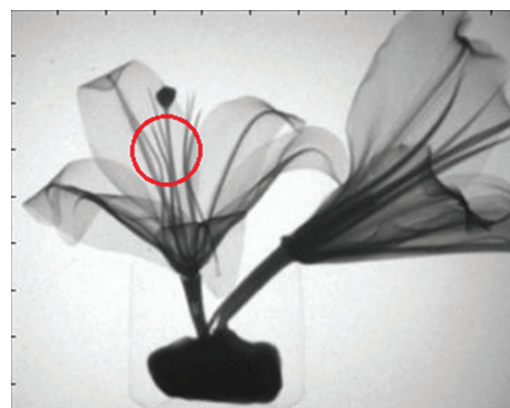
fuel and a graphite reflector. This reactor has a nominal power of 1 MW and is thus categorized under low-power research reactors. RTP possesses three radial beam ports, one tangential beam port, and one thermal column. The NR imaging facility is constructed around the radial beam port. The details are described elsewhere [14]. A total of six NR images of common objects produced at this facility are investigated, three of which are illustrated in Fig. 4.



(a)



(b)



(c)

**Fig. 4.** Examples of neutron images produced by RTP. Regions containing vague useful features are marked with solid-line circles. (a) Hard-disk drive (1509 x 1248), (b) Honeycomb (1515 x 2322), (c) Lily flower (1728 x 2132)

The remaining images are presented in Appendix III. These 16-bit images are captured at an exposure time of 300 s and they are shown here after noise removal and brightness adjustment. Figs. 4(a), 4(b), and 4(c) correspond to images of a hard-disk drive, an aircraft honeycomb, and a lily flower, respectively. The size of each image is indicated in the figure. Visually, these images are blurry, which causes difficulty in the identification of important features or useful structures. For illustration purposes, regions containing useful information are encircled with solid lines. In the case of the hard-disk-drive in Fig. 4(a), five small anomalies located on the controller unit appear faded and blurry. Fig. 4(b) illustrates the loss of minute details, such as small structures of the honeycomb. Meanwhile, left petal of a flower's image in Fig. 4(c) show fine filaments that are blurry and out of focus. The proposed deblurring method is applied to enhance the images in Fig. 4. The results are presented and discussed in next section.

## 4. RESULTS

### 4.3. DETERMINATION OF PATCH SIZE

The effect of various patch sizes and the number of iterations is investigated first. Given that the ground measurements required for such an investigation and the lack of ground truth image for NR at present, optical images are the best alternative option. The popular dataset published in [15] is considered for this purpose. This dataset includes four ground truth images (255×255) and eight PSF kernels (25×25). These ground images are blurred using eight various PSF kernels, which results in 32 blurred images. The results are evaluated in terms of the following quality indices: similar-

ity kernel ( $S(k, \hat{k})$ ), mean peak signal ratio (PSNR), and mean structural similarity (SSIM). Figs. 5–6 show the plotted results comparing the proposed method and [7]. The former reveals variation in  $S(k, \hat{k})$ , and the latter depicts the trends of PSNR and SSIM with the increase in patch size and iteration. In terms of  $S(k, \hat{k})$ , both algorithms show no considerable variation when different patch sizes are used. Only the number of iterations exhibits a crucial effect on  $S(k, \hat{k})$ , which increases with the increase in the number of iterations. This trend is expected because  $k$  approaches  $\hat{k}$  as the iteration increases. Moreover,  $S(k, \hat{k})$  converges to almost the same value for both algorithms after eight iterations (Fig. 5). A striking difference is noted upon close examination of this figure. Although the  $S(k, \hat{k})$  values calculated from the proposed approach show no significant difference from those computed in [7], the former registers slightly and consistently higher values (Figs. 5(b-c)). The same trend is achieved for SSIM, as suggested by the results in Figs. 6(a-d)(ii). The competitiveness of the proposed method is best shown in terms of the PSNR. Fig. 6 reveals the significantly higher PSNR values of the proposed method compared with those in [7], especially for smaller patch sizes. The proposed solution attains a PSNR of 29 dB compared to 26 dB in [7] for a patch size corresponding to  $SF=0.025$ . This findings translates to an approximately 11% increase in the PSNR. Results displayed in Figs. 5–6 also suggest a  $SF=0.025$  as the best patch size for the proposed method. Hence, this size is used for the restoration of NR images in Fig. 4. The results are discussed in the following subsection. Meanwhile, Appendix IV provides results obtained using an image from Levin dataset, which prove the accuracy of the proposed method in the restoration of optical or synthetic images.

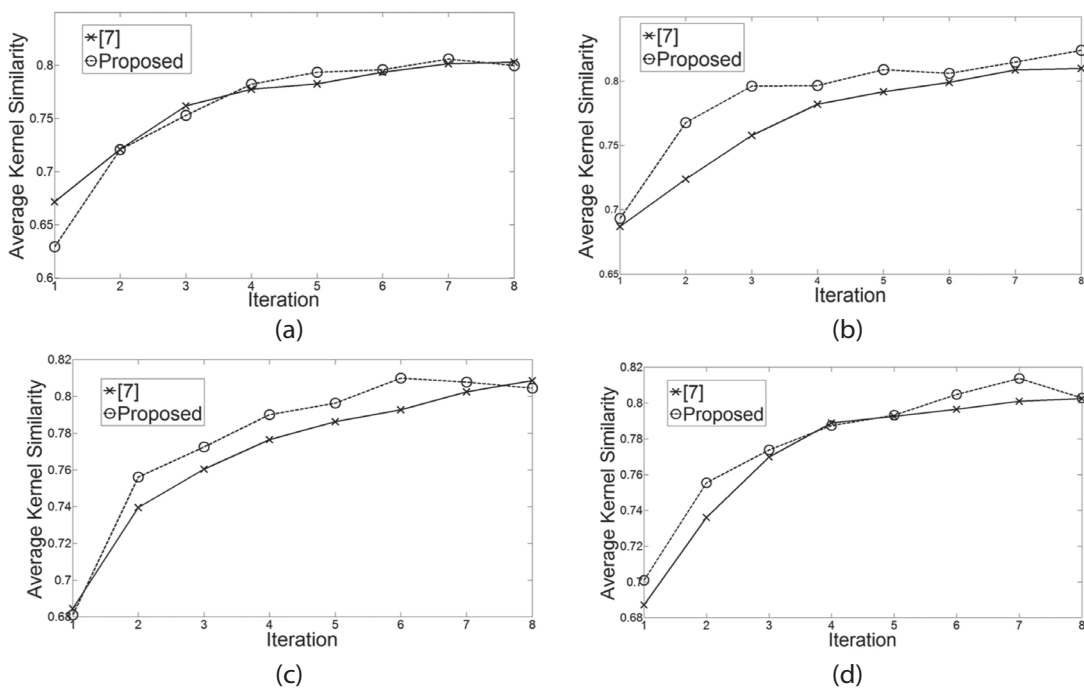
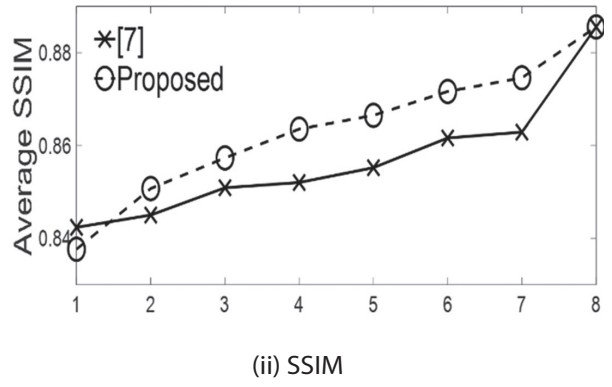
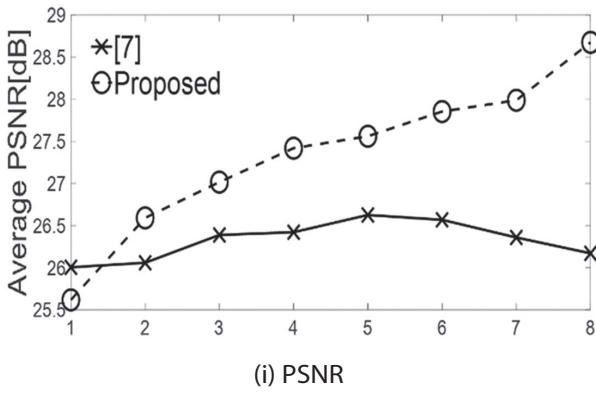
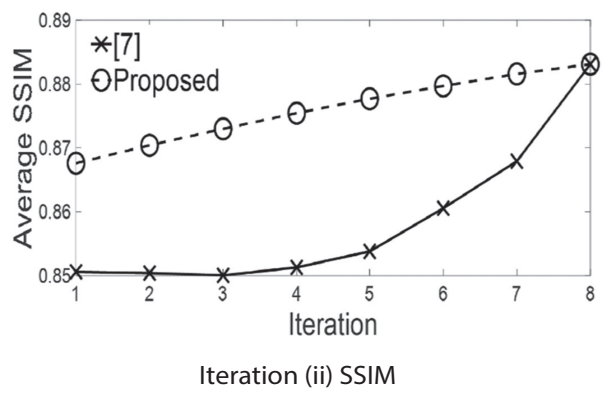
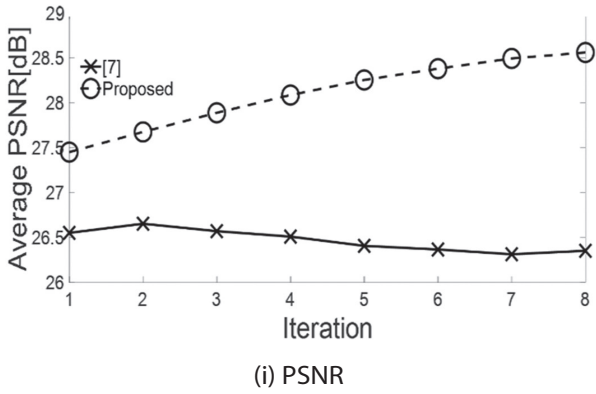


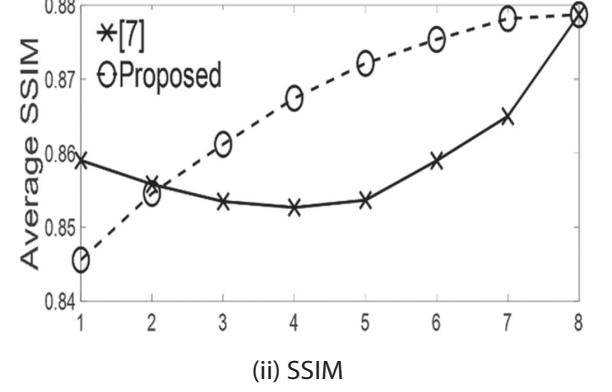
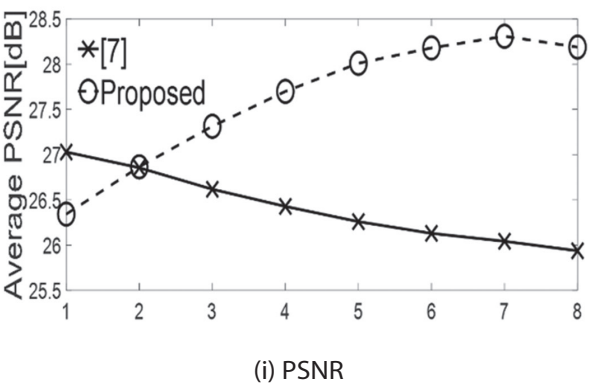
**Fig. 5.** Effect of varying patch size on PSNR and SSIM in the comparison of the proposed method and that of [7]. (a)  $SF=0.020$ , (b)  $SF=0.025$ , (c)  $SF=0.030$ , (d)  $SF=0.035$



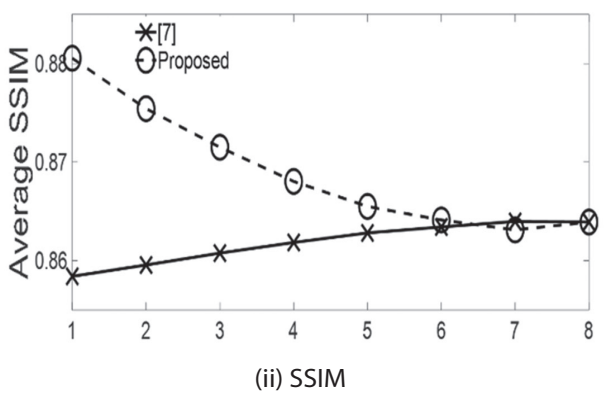
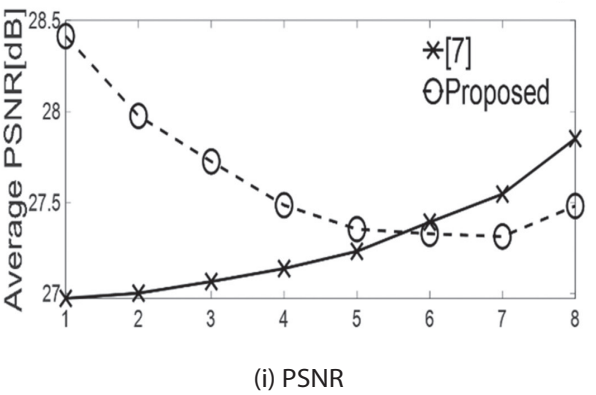
(a)



(b)



(c)



(d)

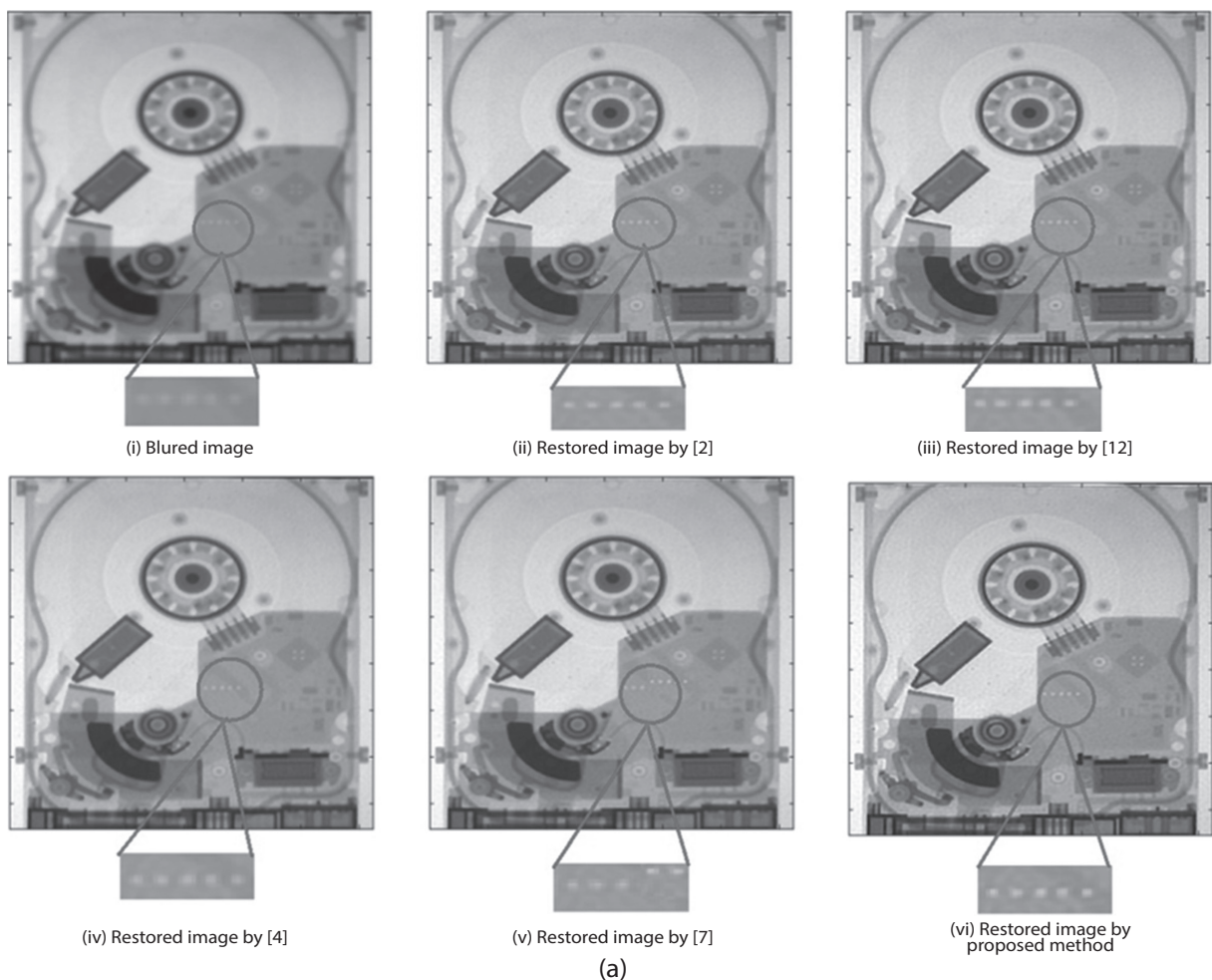
**Fig. 6.** Effect of varying patch sizes on PSNR and SSIM in the comparison of the proposed method and that of [7].  
 (a)  $SF=0.020$ , (b)  $SF=0.025$ , (c)  $SF=0.030$ , (d)  $SF=0.035$

## 4.2. IMAGE RESTORATION

The settings determined from the above investigation are used in image deblurring experiments involving the real neutron images in Fig. 4. The performance of the proposed method is first evaluated visually (Fig. 7). The figure reveals the restoration findings corresponding to six neutron images of a hard-disk, a honeycomb, lily flower, aerosol spray can, rose flower, and laptop battery pack. Selected regions are zoomed-in to highlight small and fine details. Here, restorations are performed using the parameters determined heuristically through trial-and-error experiments:  $\mu=0.004$ ,  $\gamma=2$ ,  $\beta_0=2\mu$ ,  $\beta_{max}=10^5$ ,  $\alpha=2$ ,  $\lambda=0.1$ , and  $iter_{max}=5$ . The thoroughness of investigation results are compared with those of state-of-the-art methods published in [2], [4], [7], and [12]. The default settings proposed by these authors are used in restorations.

Referring to Fig. 7(a) and Fig. 7(b), the hard-disk and honeycomb resemble images captured from natural sceneries given the possible similar grayscale values of pixels in the same area and very slow gradient changes. By contrast, rapid changes can be observed in the grayscale values of pixels located in the vicinity of dominant objects. Thus, images with such pixel values exhibit a heavy-tailed distribution and local smoothing. For this reason, their intensity distributions are highly disorganized. As a result, the restoration of these images frequently results in the presence of geometrical artifacts. Despite this diffi-

culty, overall, the proposed method produces results that are comparable to those of [7] (Figs. 7(a-b)(vi)). A close examination of Fig. 7(a)(v) reveals geometrical errors in the result produced by [7]. Visually, the locations of five small anomalies on the controller unit shifted slightly to the top. Other established methods, particularly [2], [12] and [4], resulted in blurry restoration, as evident from Figs. 7(b)(ii-iv), 7(c)(ii-iv), 7(d)(ii-iv), 7(e)(ii-iv), 7(f)(ii-iv), respectively. Although the hard-disk anomalies and fine honeycomb structures show slight improvement in their appearance, they remain blurry. Indirectly, these findings suggest that the heavy-tailed prior in [2] is an inefficient PSF estimator for textured images. Similar to the hard-disk and honeycomb, the restoration of lily flower is equally challenging because this object features a few grayscale tones during radiographical reconstruction. Such an image exhibits a low dynamic range (Fig. 7(c)(i)). As a result, the image contains very limited information that is useful for PSF estimation. Fig. 7(c)(vi) shows that the proposed method performs exceptionally well compared with other established methods. Visually, this result shows a relatively sharper and cleaner image compared with other images in the figure. In this case, the fine elements on the left side of the petal exhibit more distinct and clearer details. Other established methods also perform reasonably well, but the findings remain blurry (Figs. 7(c)(ii-iv)). The restoration of remaining images in Appendix III are shown in Appendix V. Similar trends can be observed from these results.



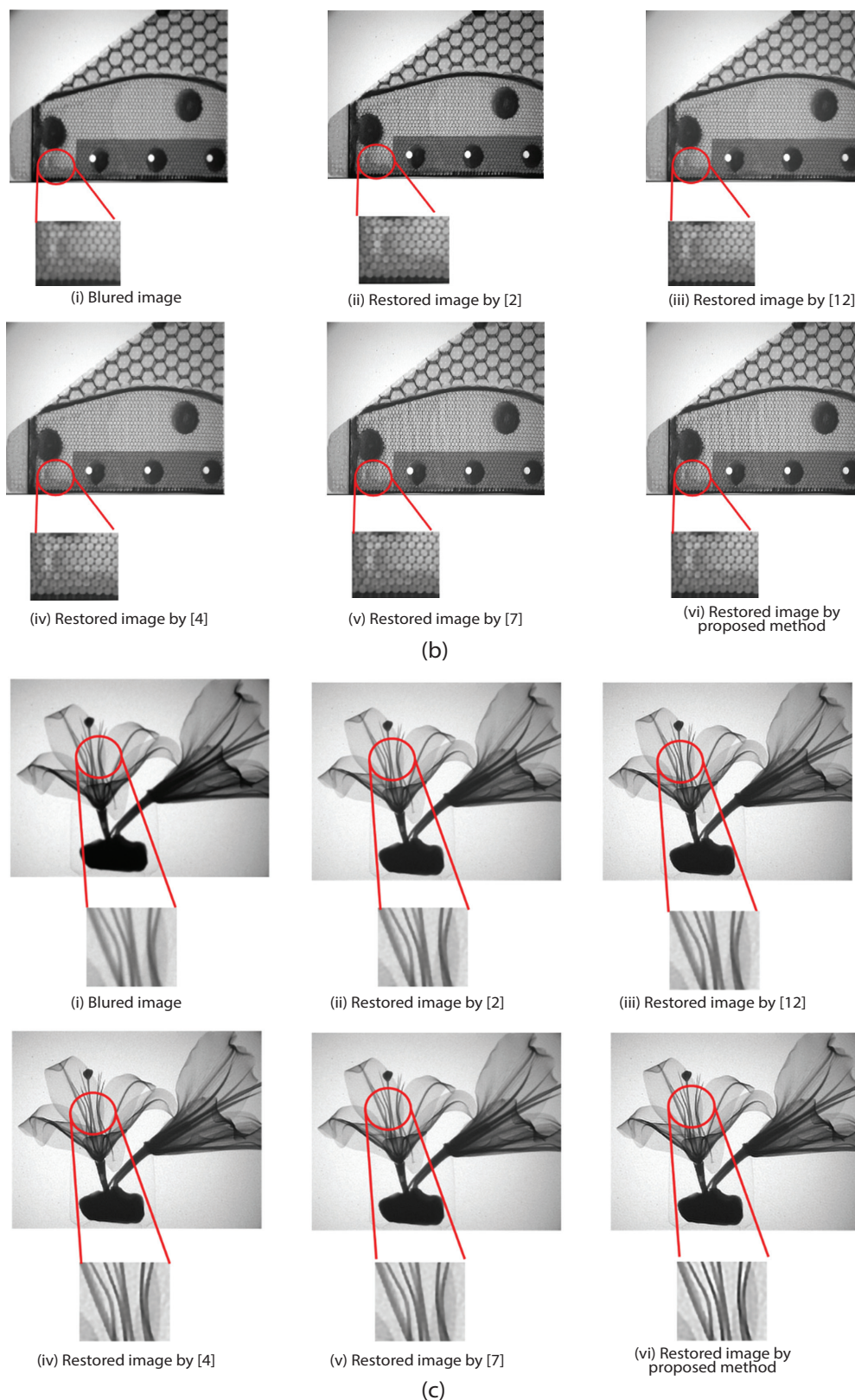


**Fig. 7.** Restoration results correspond to images in Fig. 4. (a) Hard-disk drive, (b) Honeycomb, (c) Lily flower

In addition to visual quality, the performance of the proposed method is examined quantitatively using three evaluation indices, including the Blind or Referenceless Image Spatial Quality Evaluator (BRISQUE)[16], image information entropy, and image contrast. As a unitless quality, the smaller the BRISQUE index, the better the im-

age quality. Meanwhile the image contrast is a measure of the difference in brightness between the highest and lowest gray values in an image, directly indicating the degree of gray level variation. Essentially, the larger the image contrast, the clearer the image is. The entropy, in the other hands, indicates the richness of information

or details contained in the image. In this case the larger the entropy, the more complete the image is. These metrics are calculated for all restored images used in this paper. The values are then averaged and tabulated for each method, and Table 1 summarizes the results. The BRISQUE, entropy and contrast values for each blurred image are included in the table for reference.

Referring to Table 1, overall, the proposed method offers a superior performance, which leads to the smallest and stable BRISQUE measures. On average, the proposed method attains a BRISQUE index of 46.05. The highest and hence the least accurate restoration are those from [12], with a BRISQUE index averaging 47.38. Their algorithm works well with images dominated by low-intensity pixels because it uses dark channels when enforcing the sparsity of solutions.

This condition is difficult to meet in NR because the images that produced by the algorithm usually contain many brightly illuminated pixels (Fig. 4). This finding mainly explains the reduced performance in [12]. Meanwhile, the performances of the algorithms in [4] and [7] is in between BRISQUE indices of 46.37 and 47.19, respectively. Similarly the proposed method achieved highest scores in term of entropy and contrast, averaging at 7.09 and 1.05 respectively. In comparison the algorithm of [2] resulted in the lowest entropy and contrast, averaging at 7.06 and 0.84 respectively.

The entropy and contrast values produced by other algorithms fall within this range. Like subjective evaluation, similarly, in this case the proposed method is consistently the best performing algorithm compared to established techniques.

**Table 1.** Quantitative evaluation comparing proposed and established methods.

INDEX	Images	Methods					Proposed method
		Original	[2]	[12]	[4]	[7]	
BRISQUE	Fig. 7 (a)	48.50	42.02	48.49	43.46	43.80	43.45
	Fig. 7(b)	66.86	44.44	43.60	43.50	49.50	43.50
	Fig. 7(c)	57.30	43.60	46.00	46.10	43.60	43.50
	App.III(a)	44.76	44.68	43.67	43.79	43.92	43.98
	App.III(b)	57.88	57.88	57.88	56.99	57.29	56.94
	App.III(c)	44.90	44.90	44.90	44.42	45.05	44.93
	Ave.	55.72	46.25	47.38	46.37	47.19	46.05
ENTROPY	Fig. 7 (a)	7.39	7.43	7.44	7.43	7.43	7.51
	Fig. 7(b)	7.64	7.70	7.69	7.70	7.74	7.75
	Fig. 7(c)	7.32	7.33	7.36	7.35	7.34	7.37
	App.III(a)	7.17	7.18	7.19	7.19	7.18	7.19
	App.III(b)	5.99	6.05	6.06	6.04	6.06	6.07
	App.III(c)	6.99	6.68	6.68	6.68	6.68	6.69
	Ave.	7.03	7.06	7.07	7.06	7.07	7.09
CONTRAST	Fig. 7 (a)	0.89	0.86	1.02	1.30	1.00	1.05
	Fig. 7(b)	0.87	0.87	0.93	0.97	1.33	1.35
	Fig. 7(c)	0.88	0.90	1.15	0.99	1.06	1.24
	App.III(a)	0.98	0.98	0.93	1.01	1.02	1.03
	App.III(b)	0.53	0.52	0.65	0.61	0.64	0.71
	App.III(c)	0.88	0.88	0.96	0.91	0.94	0.95
	Ave.	0.83	0.84	0.94	0.96	0.99	1.05

### 4.3. RUNTIME

Finally, the runtime performance of the proposed algorithm is evaluated in comparison with established techniques. Table 2 tabulates the results.

**Table 2.** Runtime comparing proposed and established methods

Images	Runtime (s)				
	[2]	[12]	[4]	[7]	Proposed method
Fig. 7(a)	119	293	4125	138	127
Fig. 7(b)	129	1077	4085	265	298
Fig. 7(c)	103	234	3990	284	296
App.III(a)	85	123	1501	201	136
App.III(b)	416	82	1580	112	117
App.III(c)	276	66	1364	109	111
	Mean=188 Min=85 Max=416	Mean=313 Min=66 Max=1077	Mean=2774 Min=1364 Max=4085	Mean=184 Min=109 Max=284	Mean=180 Min=111 Max=298

Referring to Table 2 it can be seen that the proposed method is the fastest algorithm with a runtime averaging at 180 s; minimum and maximum runtimes of 111 s and 298 s respectively.

Clearly the soft thresholding helps speed-up the processing since only nonzero elements are used in the computation as previously explained. In comparison the algorithm of [4] resulted in the highest runtime of 2774 s, while its minimum and maximum runtimes range from 1364 s to 2774 s. Hence, [4] is the slowest, and hence, the most complex algorithm. This is mainly due to this algorithm utilizing joint prior operation which is a very time-consuming procedure. Meanwhile the performance of other algorithms lie between the proposed method and [4] as evident from Table 2.

## 5. CONCLUSIONS

This work presented a relatively novel, simple, and effective patch-wise enhanced prior for image restoration in a blind deconvolution framework. Inspired by the decreased intensity of high-intensity pixels due to blurring, the proposed method incorporates the EPI prior in a non-overlapping patch combined with the existing image gradient prior to regularization of the solution. A coarse-to-fine adjustment with a multilayer scaling approach is implemented within the MAP framework. Overall, these steps provide an accurate estimation of PSF and hence a superior restoration performance. Experiments using real degraded neutron images produce competitively important results, visually and quantitatively. Importantly, the restored results reveal important structures and minute details in images. Hence, the proposed method can potentially improve the visibility of blurry neutron images, which is crucial in applications, such as material characterization. It also performs reasonably well in challenging problems that involved large PSF kernels. Nevertheless, the algorithm may yield dissatisfactory results for images that are severely degraded by gamma noise. Such a degradation is inherently observed in small nuclear reactors. Thus, an effective denoising strategy may be needed prior to restoration.

## 6. ACKNOWLEDGEMENTS

The work is supported by Malaysian Nuclear Agency, the Director's office of MNA, the Reactor Technology Centre, and the Technical Support Division. KY acknowledges Ministry of Higher Education Malaysia for providing scholarship enabling her to pursue post-graduate study at Universiti Sains Malaysia. This project is partly financed by Universiti Sains Malaysia (1001-PELECT.8070009).

## 7. REFERENCES:

- [1] M. Kardjilov, N. Manke, I. Woracek, R. Hilger, A. J. Banhart, "Advances in neutron imaging", *Materials Today*, Vol. 31, No. 6, 2018, pp. 652-672.
- [2] J. Kotera, F. Sroubek, P. Milanfar, "Blind deconvolution using alternating maximum a posteriori estimation with heavy-tailed priors", *Proceedings of the 15th International Conference on Computer Analysis of Images and Patterns*, York, UK, 27-29 August 2013, pp. 59-66.
- [3] L. Xu, S. Zheng, J. Jia, "Unnatural L0 sparse representation for natural image deblurring", *Proceedings of the IEEE on Computer Vision and Pattern Recognition*, Portland, OR, USA, 23-28 June 2013, pp. 1107-1114.
- [4] J. Dong, J. Pan, Z. Su, M. H. Yang, "Blind image deblurring with outlier handling", *Proceedings of the IEEE International Conference on Computer Vision*, Venice, Italy, 22-29 October 2017, pp. 2497-2505.
- [5] J. Pan, Z. Su, "Fast L0-regularized kernel estimation for robust motion deblurring", *IEEE Signal Processing Letters*, Vol. 20, No. 9, 2013, pp. 841-844.
- [6] D. Hu, J. Tan, L. Zhang, X. Ge, J. Liu, "Image deblurring via enhanced local maximum intensity prior", *Signal Processing: Image Communication*, Vol. 96, 2021, pp. 116311.
- [7] F. Wen, R. Ying, Y. Liu, T. K. Truong, "A simple local minimal intensity prior and an improved algorithm for blind image deblurring", *IEEE Transactions on Circuits and Systems for Video Technology*, Vol. 31, No. 8, 2021, pp. 2923-2937.
- [8] D. Yang, X. Wu, H. Yin, "Blind Image Deblurring via a Novel Sparse Channel Prior", *Mathematics*, Vol. 10, No. 8, 2022, pp. 1-18.
- [9] D. Zhang, G. Sun, Z. Yang, J. Yu, "A high-density gamma white spots-Gaussian mixture noise removal method for neutron images denoising based on Swin Transformer UNet and Monte Carlo calculation", *Nuclear Engineering and Technology*, Vol. 56, No. 2, 2024, pp. 715-727.
- [10] C. Zhao, W. Yin, T. Zhang, X. Yao, S. Qiao, "Neutron image denoising and deblurring based on generative adversarial networks", *Nuclear Instruments and Methods in Physics Research Section A: Accelerators, Spectrometers, Detectors and Associated Equipment*, Vol. 1055, 2023, p. 168505.
- [11] Y. Khairiah, M. Z. Abdullah, I. Haidi, "Restoration of radiographic neutron image using single-chan-

- nel blind deconvolution", International Journal of Electrical and Electronic Engineering, Vol. 13, No.2, 2024, pp. 160-167.
- [12] J. Pan, Z. Hu, Z. Su, M. H. Yang, "L0-regularized intensity and gradient prior for text images deblurring and beyond", Transactions on Pattern Analysis and Machine Intelligence, Vol. 39, No. 2, 2017, pp. 342-355.
- [13] S. Cho, S. Lee, "Fast motion deblurring", ACM Transactions on Graphics, Vol. 28, No. 5, 2009, pp. 1-8.
- [14] R. Jamro et al. "Monte Carlo Simulation for Designing Collimator of the Neutron Radiography Facility in Malaysia", Physic Procedia, Vol. 88, 2017, pp. 361-368.
- [15] A. Levin, Y. Weiss, F. Durand, W. T. Freeman, "Understanding blind deconvolution algorithms", IEEE Transactions on Pattern Analysis and Machine Intelligence, Vol. 33, No. 12, 2009, pp. 2354-2367.
- [16] A. Mittal, A. K. Moorthy, A. C. Bovik, "No- Reference Image Quality Assessment in the Spatial Domain", IEEE Transactions on Image Processing, Vol. 21, No. 12, 2012, pp. 4695-4708,.

## APPENDIX I.

The main steps involved in solving  $L$  and  $k$  subproblems are summarized in Algorithms 1 and 2, respectively. In the latter case, the main parameter  $\gamma$  is set to 2.

---

### Algorithm 1 $L$ subproblem

---

**Input:** Downscaled blurred image  $B$ , interim kernel  $k^i$

$\beta \leftarrow \beta_0, L^0 \leftarrow B$

**While**  $\beta \leq \beta_{max}$ , **do** ( $t=0,1,2,\dots$ )

$L^{t+1,0} \leftarrow L^t$

**For**  $j=0:J-1$  **do**

Obtain  $\tilde{L}_s^{t+1,j}$  via Equation (16)

Compute  $M^{t+1,j}$  via Equation (17)

Update  $\tilde{L}^{t+1,j}$  via Equation (19)

Calculate gradient thresholding to obtain  $G^{t+1,j+1}$  via Equation (21)

Update  $L^{t+1,j+1}$  via Equation (23)

**End of**

$\tilde{L}^{t+1} \leftarrow L^{t+1,j}$

$\beta \leftarrow a\beta$

**End while**

$L^{i+1} \leftarrow L^{t+1}$

**Output:** Intermediate latent image estimation  $L^{i+1}$

---



---

### Algorithm 2 $k$ subproblem

---

**Input:** Blurred image  $B$

Initialize  $k^0$  from the previous layer of pyramid

**For**  $i=1:iter_{max}$  **do**

Estimate  $L^i$  via Algorithm 1 using  $k^{i-1}$

Estimate  $k^i$  via Equation (25)

**End For**

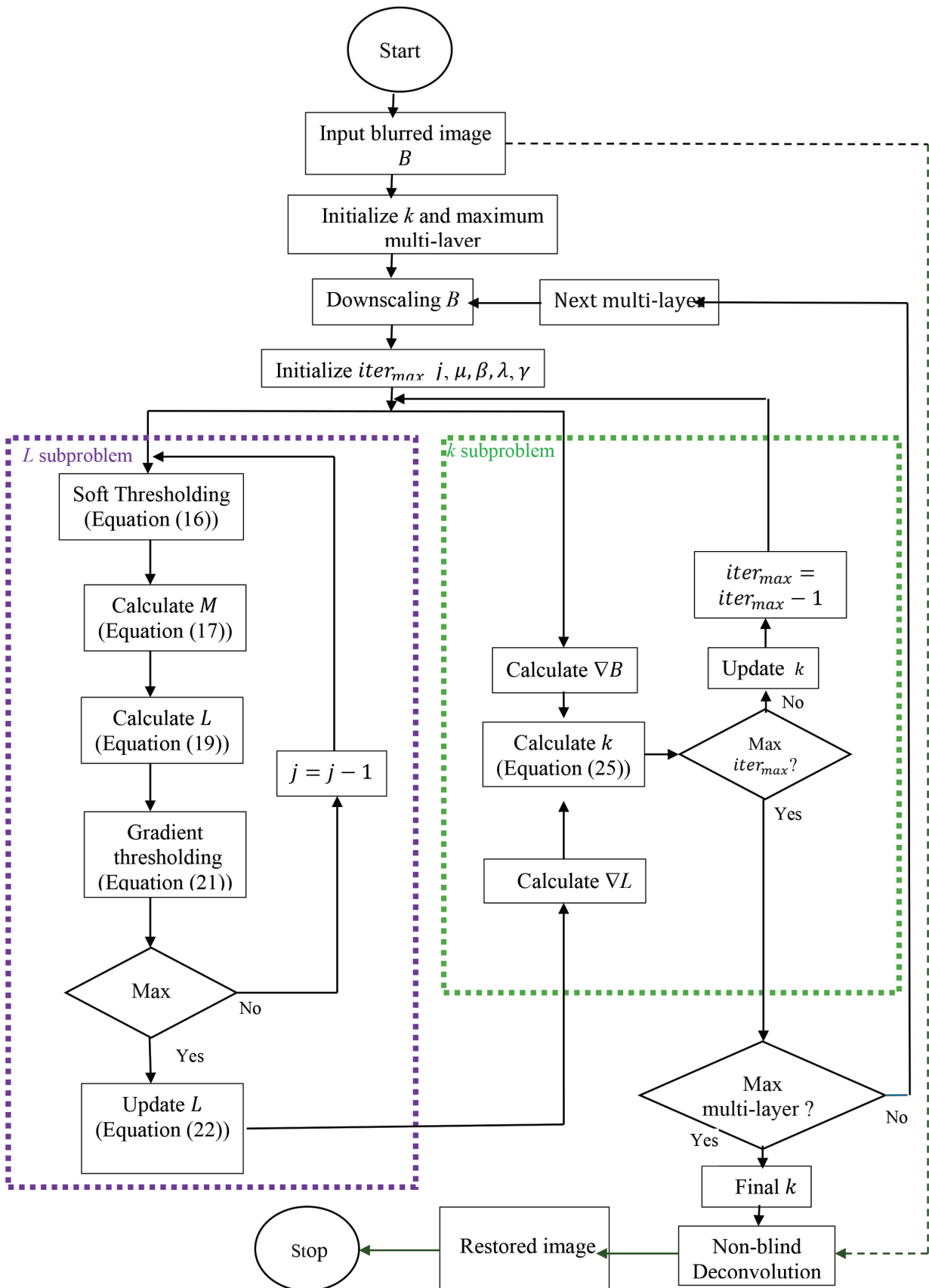
$\hat{k} \leftarrow k^i, \hat{L} \leftarrow L^i$

**Output:** estimated PSF  $\hat{k}$ , intermediate image  $\hat{L}$

---

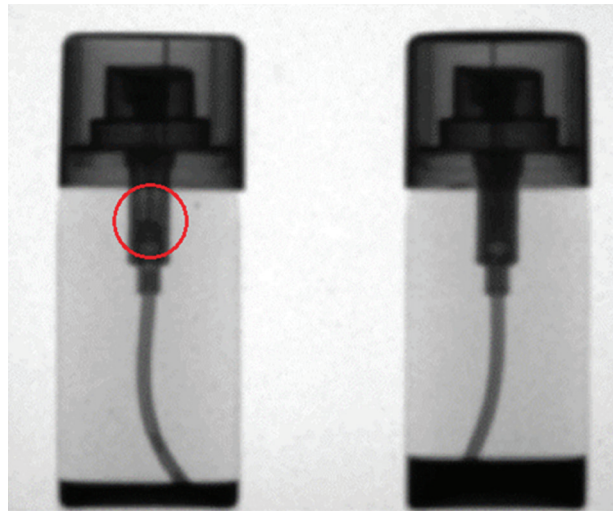
**APPENDIX II.**

Detailed flowchart of the algorithm for solving  $L$  and  $k$  subproblems. The dotted line indicates subsequent processing following all major calculations (solid lines).



### APPENDIX III.

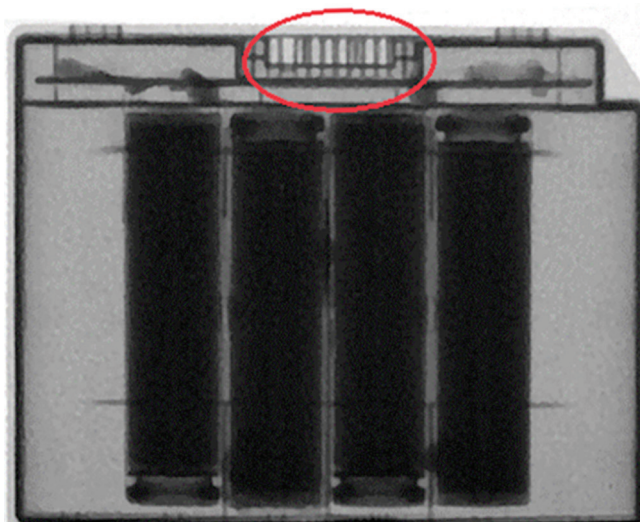
Another three examples of blurry neutron images of three common objects produced by RTP. Regions containing vague useful features are marked with solid-line circles.



(a) Aerosol spray can (1180 x 1380)



(b) Rose Flower (1143 x 1509)



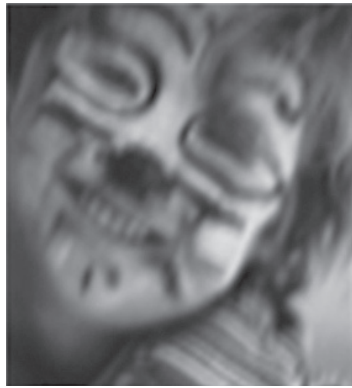
(c) Laptop battery pack (966 x 1734)

#### APPENDIX IV.

Example of a deconvolution result from Levin's dataset showing (a) the ground truth and (b) the blurred version of (a). (c), (d), (e), (f), and (g) Restored images produced using the methods of Kotera et al. (2013), Pan et al. (2017), Dong et al. (2017), and Wen et al.(2021), and the proposed method, respectively.



(a)



(b)



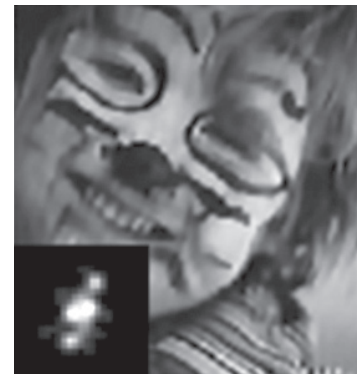
(c)  $s(k, \hat{k})$  0.69, PSNR 28.5 dB  
SSIM 0.87



(d)  $s(k, \hat{k})$  0.69, PSNR 30.1 dB  
SSIM 0.90



(e)  $s(k, \hat{k})$  0.63, PSNR 29.3 dB  
SSIM 0.65



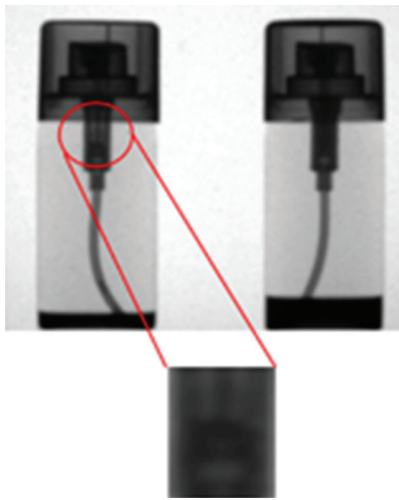
(f)  $s(k, \hat{k})$  0.63, PSNR 27.5 dB  
SSIM 0.87



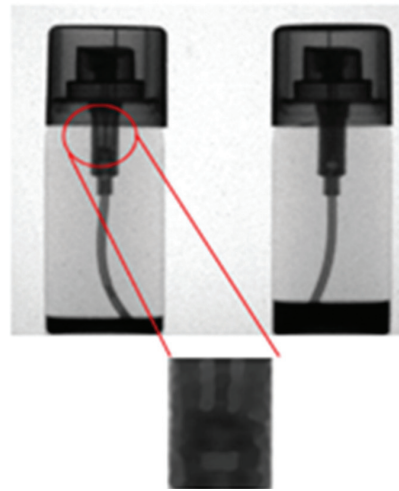
(g)  $s(k, \hat{k})$  0.73, PSNR 30.1 dB  
SSIM 0.90

**APPENDIX V.**

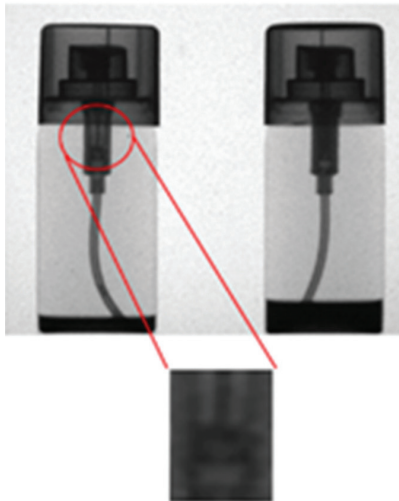
Restoration results correspond to images in Appendix III.



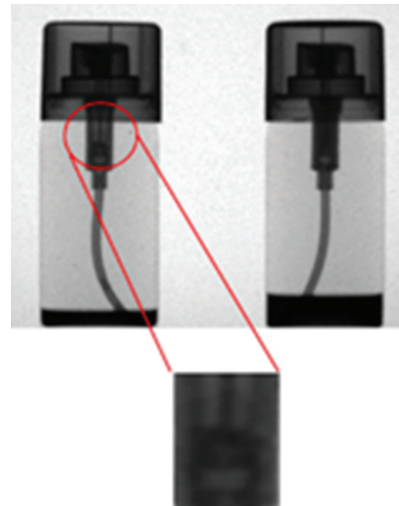
(i) Blurred image



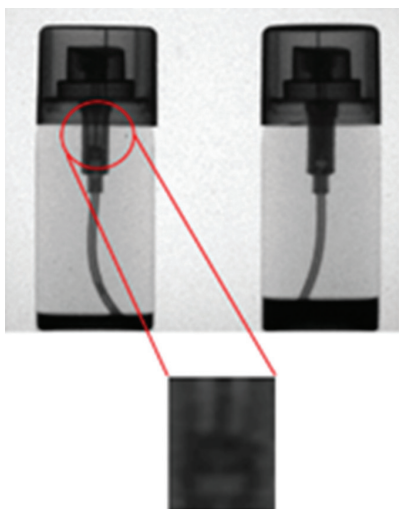
(ii) Restored image by [2]



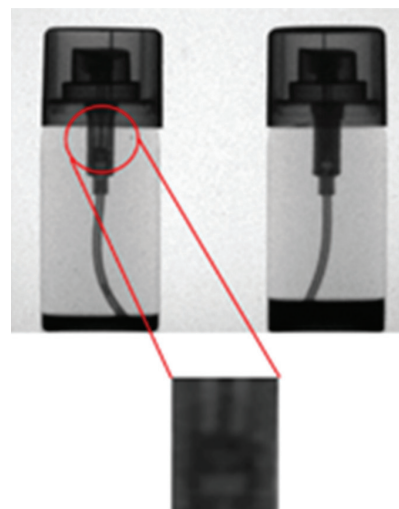
(iii) Restored image by [12]



(iv) Restored image by [4]

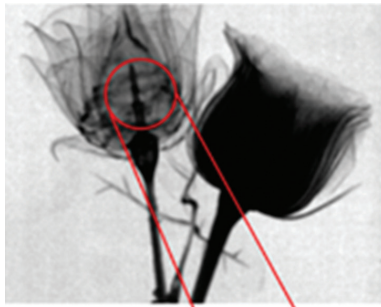


(v) Restored image by [7]

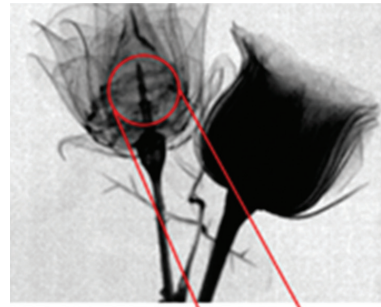


(iii) Restored image by proposed method

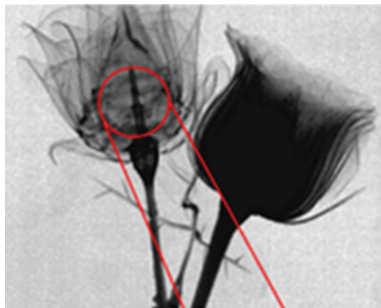
(a) Aerosol spray can



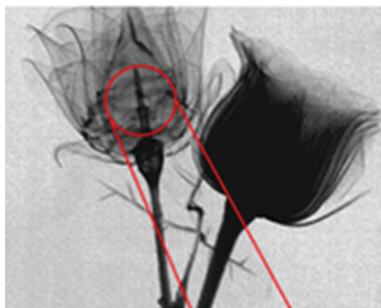
(i) Blurred image



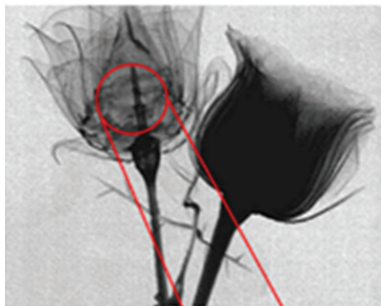
(ii) Restored image by [2]



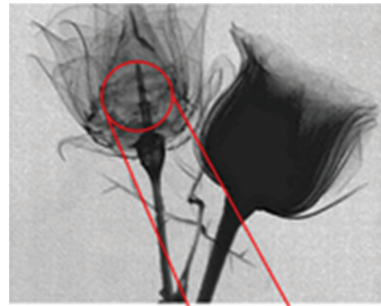
(iii) Restored image by [12]



(iv) Restored image by [4]

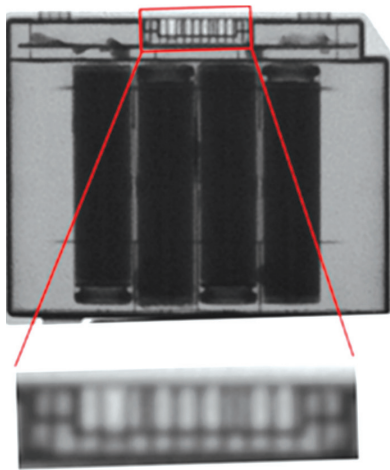


(v) Restored image by [7]

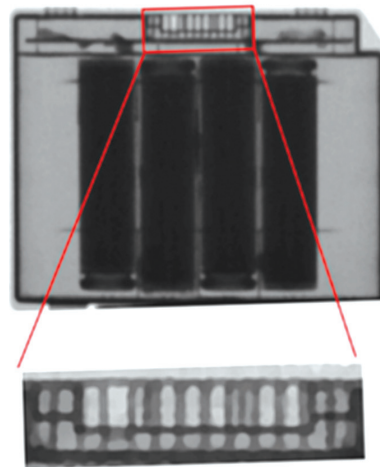


(iii) Restored image by proposed method

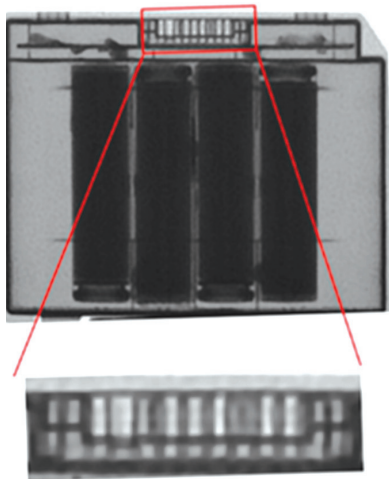
(b) Rose flower



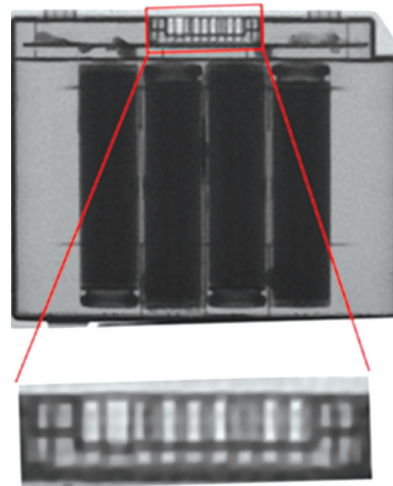
(i) Blurred image



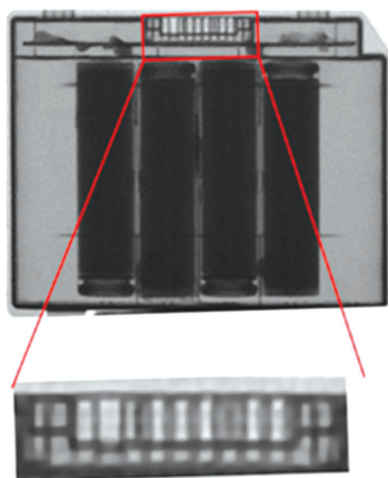
(ii) Restored image by [2]



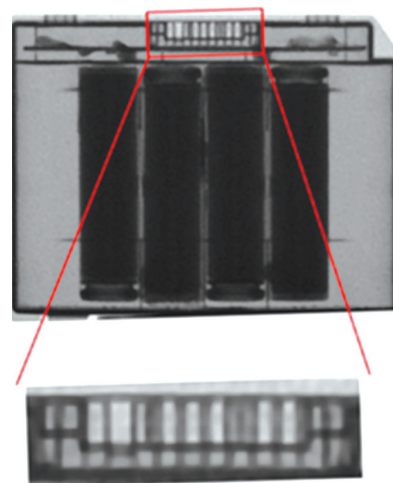
(iii) Restored image by [12]



(iv) Restored image by [4]



(v) Restored image by [7]



(iii) Restored image by proposed method

(c) Laptop battery pack